RESEARCH ARTICLE

Tailored Design of a Water-Based Nanoreactor Technology for Producing Processable Sub-40 Nm 3D COF Nanoparticles at Atmospheric Conditions

Gemma Llauradó-Capdevila, Andrea Veciana, Maria Aurora Guarducci, Alvaro Mayoral, Ramon Pons, Lukas Hertle, Hao Ye, Minmin Mao, Semih Sevim, David Rodríguez-San-Miguel, Alessandro Sorrenti, Bumjin Jang, Zuobin Wang, Xiang-Zhong Chen, Bradley J. Nelson, Roc Matheu, Carlos Franco,* Salvador Pané,* and Josep Puigmartí-Luis*

Covalent organic frameworks (COFs) are crystalline materials with intrinsic porosity that offer a wide range of potential applications spanning diverse fields. Yet, the main goal in the COF research area is to achieve the most stable thermodynamic product while simultaneously targeting the desired size and structure crucial for enabling specific functions. While significant progress is made in the synthesis and processing of 2D COFs, the development of processable 3D COF nanocrystals remains challenging. Here, a water-based nanoreactor technology for producing processable sub-40 nm 3D COF nanoparticles at ambient conditions is presented. Significantly, this technology not only improves the processability of the synthesized 3D COF, but also unveils exciting possibilities for their utilization in previously unexplored domains, such as nano/microrobotics and biomedicine, which are limited by larger crystallites.

1. Introduction

Nature can precisely control the assembly and growth of crystalline structures across scales, from the nano- to the millimeter scale, to achieve materials with targeted functions while using only a limited selection of components and/or building blocks.[1] Despite the significant progress made by the scientific community in the development of crystalline synthetic materials, the methods and technologies used still pale in comparison to the workings of nature.[2,3] For instance, most attempts made at controlling the assembly, size, and function of human-made crystalline materials have been based on Edisonian

G. Llauradó-Capdevila, J. Puigmartí-Luis
Departament de Ciència de Materials i Química Física
Institut de Química Teòrica i Computacional
Universitat de Barcelona
Barcelona 08028, Spain
E-mail: josep.puigmarti@ub.edu

A. Veciana, L. Hertle, H. Ye, M. Mao, S. Sevim, X.-Z. Chen, B. J. Nelson, C. Franco, S. Pané
Institute of Robotics and Intelligent Systems ETH Zurich
Tannenstrasse 3, Zurich CH 8092, Switzerland
E-mail: carlos.franco@chem.ethz.ch; vidalp@ethz.ch

M. A. Guarducci
Dipartimento di Chimica e Tecnologie del Farmaco
Sapienza Università di Roma
Roma 00185, Italy

A. Mayoral
Instituto de Nanociencia y Materiales de Aragón (INMA)
CSIC-Universidad de Zaragoza
Zaragoza 50009, Spain

R. Pons
Institute for Advanced Chemistry of Catalonia (IQAC–CSIC)
Barcelona 08034, Spain

D. Rodríguez-San-Miguel
Departamento de Química Inorgánica
Universidad Autónoma de Madrid
Madrid 28049, Spain

A. Sorrenti
Departament de Química Inorgànica i Orgànica (Secció de Química Orgànica)
Institut de Química Teòrica i Computacional
Universitat de Barcelona
Barcelona 08028, Spain

B. Jang
Department of Robotics
Hanyang University ERICA Campus
Ansan-si 15588, Republic of Korea

**ADVANCED
SCIENCE NEWS**

www.advancedsciencenews.com

**ADVANCED
MATERIALS**

www.advmat.de

experimentation, in which parameters such as the molecular design, solvent, temperature, catalyst concentration, and/or monomer composition are varied individually, and in discrete steps, to achieve the most stable thermodynamic product, striving for the desired size and structure, both of which are crucial for enabling a specific function.[4,5]

Covalent organic frameworks (COFs) stand as an outstanding showcase of these human-engineered crystalline materials and underlying Edisonian approach. COFs are porous crystalline structures assembled in 2D and 3D through covalent bonds.[6] Note that when crystals are solely grown from covalent bonds, they often yield kinetically trapped disordered structures.[7,8] To avoid this, solvothermal conditions and reversible covalent bonds have become prevalent in the COF field to foster the generation of porous crystalline thermodynamic products.[9,10] Yet, however, COF synthesis methods often rely on the use of hazardous or toxic solvents as reaction media, where the solubility of the building blocks is severely limited.[11,12] This limitation frequently results in the formation of irregular and unprocessable microcrystalline powders where the control over their morphology and size is greatly hampered.[13] While significant advancements have been made in the synthesis and processing of 2D COFs by effectively controlling their formation across various scales,[14] the development of 3D COF crystals of varying sizes is still challenging, significantly impeding their processability and constraining their widespread application beyond the realms of catalysis and adsorption.[15] Recently, the use of modulators during the synthesis of 3D COFs enabled the generation of single crystals measuring several tens of micrometers in size.[16] This innovative approach demonstrated that modulators can effectively inhibit the rapid nucleation of 3D COFs and concurrently act as error-correction moieties during crystal growth, enabling the generation of large single crystals suitable for single-crystal X-ray diffraction analysis.[16] Yet, this synthetic approach relies on harsh conditions that hinder the controlled assembly of these materials at

the nanoscale, which is crucial for improving their processability and seamless integration into micrometric structures.[17] To the best of our knowledge, no existing methodologies have been reported so far that can achieve the controlled assembly of 3D COFs at the nanoscale and under mild conditions. Such advancements are not only expected to enhance their processability, but also open new opportunities for the application of these functional materials in other fields such as nano/microrobotics and biomedicine.[18,19]

Herein, we present a water-based nanoreactor technology for producing processable sub-40 nm 3D COF nanoparticles at room temperature and atmospheric pressure. This technology relies on a micellar approach that guarantees the solubility of the 3D COF precursors in water. Our findings showcase that employing this approach allows for an in-depth examination of the growth mechanism of a 3D COF, and it also enables the production of a final colloidal solution that can be directly utilized for functionalizing intricate micrometer-sized structures with 3D COF nanoparticles, all in a convenient one-pot process.

2. Results and Discussion

We selected COF-300 as the model system to investigate and evaluate the efficacy of our water-based nanoreactor technology. In a typical synthetic process, we prepared a *catanionic* micellar media by mixing the cationic hexadecyltrimethylammonium bromide (CTAB) and anionic sodium dodecyl sulfate (SDS) surfactants in a 96:4 CTAB/SDS ratio (**Figure 1A,B**). The ratio was optimized to promote the formation of micellar assemblies with lower curvature, thereby facilitating the colloidal stabilization of the 3D COF precursors in water, namely of tetrakis(4-aminophenyl)methane (TAM) and 1,4-benzenedicarboxaldehyde (BDA) (Figure 1C), and maintaining a constant colloidal size (Table S1, Supporting Information). This approach yielded two colorless homogeneous solutions where the TAM and BDA were encapsulated within the hydrophobic core of the CTAB/SDS mixed micelles. Dynamic light scattering (DLS) measurements showed that both TAM and BDA loaded micellar aggregates had hydrodynamic diameter mean values of 2.4 and 3.3 nm, respectively (Figure S1, Supporting Information). Notably, these values were similar to those observed for the pure CTAB/SDS micelles.[20] This observation confirms that the mixed micelles remained largely unaffected by the process of solubilizing the 3D COF precursors. Upon the mixing of both micellar solutions and with the addition of acetic acid as a catalyst (0.3 M), a color change was observed in the reaction mixture, which turned to yellow (see the Supporting Information for further details of the synthesis). This color change indicated the formation of imine bonds between the two COF precursors. Moreover, the formation of larger colloidal species was confirmed by the observation of a distinct Willis–Tyndall scattering behavior, when the reaction media was irradiated using a 630 nm red laser (Figure 1F, left). Surprisingly, the resulting yellowish solution demonstrated remarkable colloidal stability, persisting without any observed precipitates even after a span of 10 days after its synthesis (Figure 1D).

With the objective of studying and understanding the reaction process within the core of the CTAB/SDS micelles, the effect of acetic acid as the catalyst of the Schiff-base reaction in the micellar media was systematically studied while keeping all
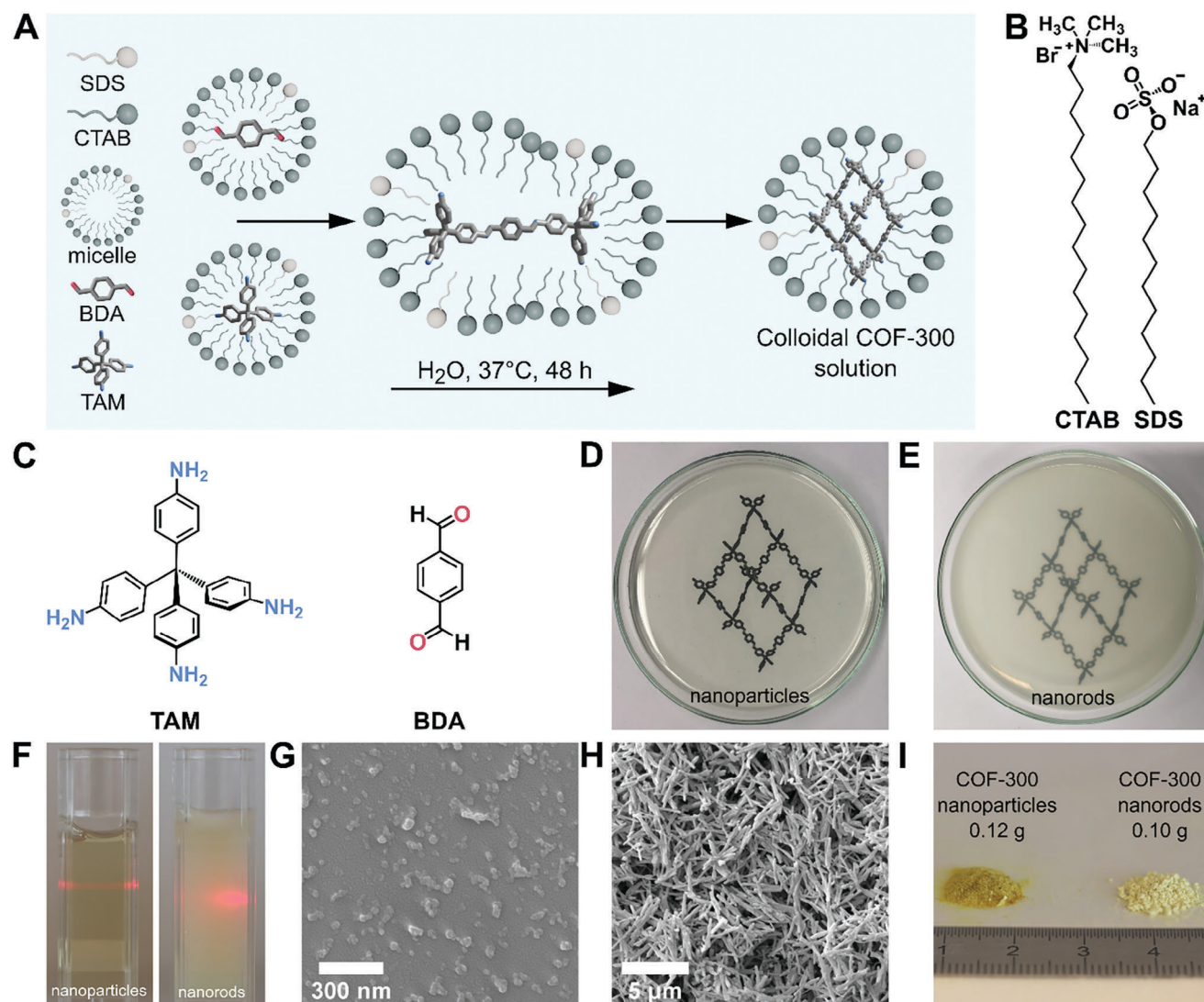
Z. Wang
International Research Centre for Nano Handling and Manufacturing of China
Changchun University of Science and Technology
Changchun 130022, China

Z. Wang
Zhongshan Institute of Changchun University of Science and Technology
Zhongshan 528437, China

X.-Z. Chen
Institute of Optoelectronics
State Key Laboratory of Photovoltaic Science and Technology
Shanghai Frontiers Science Research Base of Intelligent Optoelectronics and Perception
Fudan University
Shanghai 200433, P. R. China

R. Matheu
Departament de Química Inorgànica i Orgànica
Institut de Química Teòrica i Computacional
Universitat de Barcelona
Barcelona 08028, Spain

J. Puigmartí-Luis
Institució Catalana de Recerca i Estudis Avançats (ICREA)
Pg. Lluís Companys 23
Barcelona 08010, Spain

**ADVANCED
SCIENCE NEWS**

www.advancedsciencenews.com

**ADVANCED
MATERIALS**

www.advmat.de

Figure 1. A) Illustration of the micellar approach used to fabricate COF-300 at the nanoscale. B) Chemical structure of the cationic hexadecyltrimethylammonium bromide (CTAB) and anionic sodium dodecyl sulfate (SDS) surfactants. C) Chemical structure of the tetrakis(4-aminophenyl)methane (TAM) and 1,4-benzenedicarboxaldehyde (BDA) precursors. D,E) Micrographs of the colloidal micellar solutions obtained with a low and high catalyst concentration, respectively. The pictures were captured 4 h after the start of the reaction. F) Images of the Tyndall effect on the colloidal solutions of the nanoparticles (left) and nanorods (right) taken after 10 days of the reaction. G) SEM image of the flocculated COF-300 nanoparticles. H) SEM image of the flocculated nanorods. I) Image of the resulting yellow powders after removing the CTAB/SDS surfactants from the media.

other synthetic parameters unchanged (see Figures S2, S3, S4 and Table S2, Supporting Information). The decision to increase the catalyst concentration was driven by previous studies that have demonstrated the pivotal role of increasing the catalyst concentration in achieving high yields and promoting crystallinity in the resulting COF powders.[21,22] We observed that by doubling the catalyst concentration (0.5 M under identical synthetic conditions, a noticeable increase in turbidity was evident in the yellowish reaction mixture (Figure 1E). The Tyndall effect exhibited by this solution demonstrated an increased scattering phenomena after only 4 h of reaction, suggesting the formation of larger aggregates (Figure 1F, right). To explore the morphology of the distinct aggregates formed under different catalyst concentrations, we conducted scanning electron microscopy (SEM) analysis on

the flocculated and dried samples (see the Supporting Information for further details of sample preparation). At lower catalyst concentrations, SEM images revealed the formation of spherical-like particles with sizes below 40 nm (Figure 1G). Surprisingly, the morphology of the resulting aggregates can be significantly influenced by the catalyst concentration when utilizing the micellar approach. As depicted in Figure S3 (Supporting Information), a critical concentration is reached at 0.405 M, where a combination of nanoparticles and nanorods is observed. Subsequently, as the catalyst concentration surpasses this threshold, higher concentrations exclusively led to the development of larger nanorod structures, characterized by widths below 70 nm and lengths below 1500 nm (Figure 1H). Remarkably, this observation underlines the significance of the micellar approach in achieving

ADVANCED
SCIENCE NEWS
www.advancedsciencenews.com

ADVANCED
MATERIALS
www.advmat.de
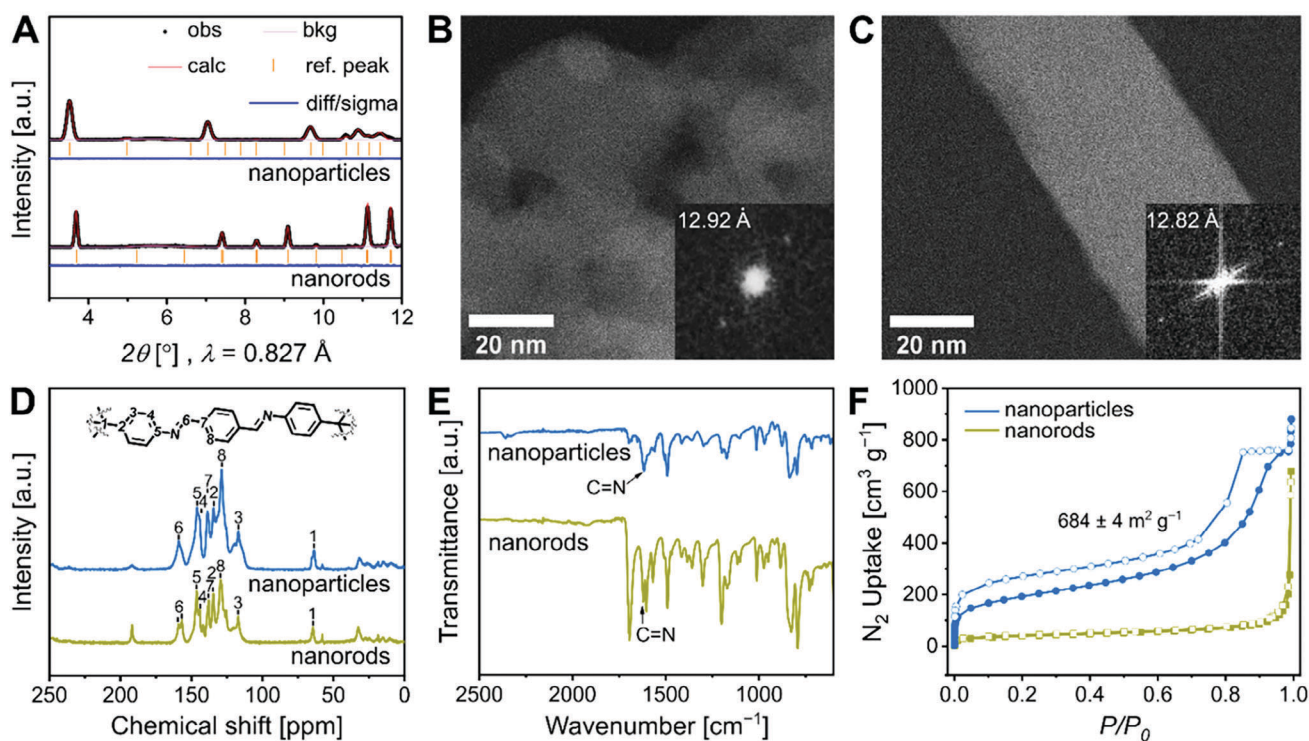
Figure 2. A) Pawley refinement of synchrotron X-ray diffraction measurements of the flocculated nanoparticles and nanorods. The observed measurement (black) matches well with the calculated data (red). The background (purple), the reference peaks (orange), and the difference between the observed and the calculated data (blue) are also depicted in the graph. The refinement yielded to a $R_w = 23.4\%$, and unit-cell parameters ($I4_1/a$) of $a = 26.90$ Å, $c = 7.44$ Å for the nanoparticles. B) Cs-corrected STEM images of flocculated COF-300 nanoparticles with 30 nm diameter and magnified HR-TEM image of the defined area with a measured d-spacing of 12.92 Å. C) Cs-corrected STEM images of flocculated nanorods with 40 nm diameter in width and magnified HR-TEM image of the defined area with measured d-spacing of 12.82 Å. D) ^{13}C CP-MAS NMR spectra of COF-300 nanoparticles (blue) and nanorods (yellow), indexed according to the literature. E) ATR-FTIR spectra of COF-300 nanoparticles (blue) and nanorods (yellow), evidencing the C=N imine stretching band. F) Nitrogen gas sorption (filled dots and squares) and desorption (unfilled dots and squares) of COF-300 nanoparticles and nanorods, respectively, at 77 K.

morphological changes. Moreover, it is important to note that conventional bulk synthetic protocols, which lack the utilization of this micellar approach, do not offer the same level of control over the morphogenesis of the resulting products, even when attempting to increase the catalyst concentration.[22] However, it is important to highlight that a lower yield is achieved when a higher catalyst concentration is used (as seen in Table S2, Supporting Information). Nevertheless, all conditions resulted in the successful generation of gram-scale yellow powders, as illustrated in Figure 1I.

To validate that the obtained aggregates correspond to COF-300, we conducted synchrotron X-ray diffraction measurements on both yellow powders (**Figure 2A**). The acquired diffraction data were subjected to fitting using the Pawley refinement method, employing the reported structural model as a reference.[23,24] While the observed diffraction pattern of the nanoparticles with peaks at 2θ ($\lambda = 0.827$ Å) = 3.52° (200), 4.96° (220), 7.05° (400), 9.67° (411), 10.57° (600), and 10.87° (501) can be assigned to the well-defined COF-300 structure, which crystallizes in the $I4_1/a$ space group,[16] the nanorods exhibit a distinct diffraction pattern that cannot be assigned to any reported structure despite their evident crystalline nature with observable peaks at 2θ $_{(\lambda = 0.827\ Å)}$ = 3.69°, 7.41°, 8.30°, 9.10°, 9.82°, and 11.13°. In addition, the re-

finement of COF-300 nanoparticles yielded a unit cell parameter of $a = b = 26.89\ 877$ Å, $c = 7.43\ 909$ Å and a unit-cell volume of 5382.5 Å³ (see Table S3, Supporting Information). Accordingly, and considering the diamond topology associated to COF-300 and the aforementioned body-centered tetragonal space group, we observed that the obtained parameters for the nanoparticles closely correspond to a diamond net with sevenfold interpenetration (*dia-c7*), in which the degree of interpenetration (N) was determined with the unit cell parameters (see Equation (S1) in the Supporting Information).[25,26]

The analysis using powder X-ray diffraction (PXRD) further confirmed the successful generation of COF-300 using the micellar approach at lower catalyst concentration (Figure S5, Supporting Information), despite the lower resolution of the XRD diffraction patterns. In contrast, when using the higher catalyst concentration (Figure S6, Supporting Information), the XRD pattern acquired from the resulting yellow powder did not correspond to the crystalline structure of COF-300, providing additional support to the synchrotron XRD measurements.

Spherical aberration corrected (Cs-corrected) scanning transmission electron microscopy (STEM) studies further validated the observations made through SEM analysis, synchrotron X-ray diffraction measurements, and/or PXRD analysis. STEM

**ADVANCED
SCIENCE NEWS**

www.advancedsciencenews.com

**ADVANCED
MATERIALS**

www.advmat.de

images clearly show the formation of spherical nanoparticles with a diameter below 40 nm, as well as nanorods exhibiting widths ranging from 35 to 65 nm and lengths between 1000 and 1500 nm (Figure 2B,C; and Figure S7, Supporting Information), values that align well to those obtained with SEM. The insets of Figure 2B,C present high-resolution (HR) STEM images and FFTs, which reveal distinct lattice fringes with a *d*-spacing of 12.93 Å for the nanoparticles and 12.82 Å for the nanorods. These lattice fringes clearly confirm the crystalline nature of the nanoparticles and nanorods, with the nanoparticles exhibiting a lattice fringe corresponding to the 200-crystal lattice plane.[16]

Moreover, the successful formation of the imine bond in both the nanoparticles and nanorods was confirmed using solid-state cross-polarization magic angle spinning nuclear magnetic resonance (^{13}C CP-MAS NMR) spectroscopy. The NMR spectra displayed clear signals indicating the presence of the imine bond. Specifically, in the case of the nanoparticles, a signal was observed at 158.7 ppm, while for the nanorods, the signal appeared at 159.0 ppm (Figure 2D; and Table S4, Supporting Information). Additionally, attenuated total reflectance Fourier-transform infrared (ATR-FTIR) spectroscopy was also employed to further confirm the presence of the imine bond in the nanoparticles and nanorods with the observation of the characteristic C=N stretching band located at 1616 and 1621 cm^{-1}, respectively (Figure 2E).

To investigate whether these morphological variations translate into distinct physico-chemical properties, thermogravimetry analysis (TGA) and nitrogen sorption isotherm measurements were performed on the two yellow powders. While the TGA thermograms of the nanoparticles align well with the previously reported COF-300, confirming the high structural stability (>500 °C) of the obtained nanoparticulated material (Figure S8A, Supporting Information), the nanorods exhibit a relatively lower thermal stability. This is evident from the weight loss of 6.20% observed between 350 and 500 °C, which can be attributed to the presence of guest COF oligomers within the structure (Figure S8B, Supporting Information).[27] Moreover, nitrogen sorption isotherm measurements of the previously activated COF-300 nanoparticles confirm their porosity. The results were adjusted to the Brunauer–Emmett–Teller (BET) model, indicating a mesoporous material with a BET surface area of 684 ± 4 m^2 g^{-1} (Figure 2F). The isotherm also displayed a hysteresis loop, indicating a dynamic behavior of the material in response to variations in gas pressure. However, note that the nanorods exhibited a lower porosity (138 ± 1 m^2 g^{-1}) which can be attributed to the different crystal structure, as confirmed with the synchrotron XRD measurements and PXRD analysis. Consequently, the characterization of the assemblies generated with the micellar approach reveal that increasing the catalyst concentration in the reaction media does not only change the morphology and crystalline structure of the final assemblies, but also has an impact on their physico-chemical properties. This finding highlights the unique advantages of the micellar approach over conventional flask mixing experiments, where such morphological control and transformation of structure and properties are challenging to achieve solely modifying the catalyst concentration.

To gain deeper insights into the influence of the environmental reaction conditions in the synthesis of COF-300 using the micellar approach, we conducted additional investigations to examine the effects of a modulator. As indicated above, modulators are commonly employed during the synthesis of COFs to improve crystallinity, reduce defect density, and facilitate the formation of larger single crystals.[16] To explore the impact of a modulator in our *catanionic* micellar mixture, we introduced aniline into the reaction media. Aniline is a well-known modulator in COF-300 synthesis;[16] however, its solubility in the micellar mixture was found to be limited at a catalyst concentration below 0.3 M. Therefore, to ensure the preparation of a homogeneous micellar solution, we increased the catalyst concentration to 0.75 M (see the Supporting Information for further details of the synthesis). Upon mixing the micellar media containing the COF-300 precursors, aniline, and acetic acid, a distinct color change was also observed in the reaction media. The previously colorless solutions transformed into a yellowish colloidal dispersion. The confirmation of colloid formation was achieved by observing the characteristic Willis–Tyndall scattering behavior when the solution was exposed to a 630 nm red laser. Notably, the colloidal solution obtained with the addition of aniline also exhibited remarkable stability, remaining unchanged even after 10 days since its synthesis (Figure S9D, Supporting Information). The stability of the resulting colloid suggested the possible formation of nanoparticles, even though the catalyst concentration was high. To investigate the morphology of the colloidal aggregates generated in the yellow colloidal solution, we performed SEM analysis of the yellow powder obtained after subsequent flocculation, washing, and drying steps (see the Supporting Information for further details of sample preparation). The data obtained revealed the presence of spherical-like particles with diameters below 40 nm, see Figure S10 (Supporting Information). In addition, the synchrotron and powder XRD patterns (Figures S11 and S12 (Supporting Information), respectively) of this yellow powder exhibited clear similarities to those obtained for the COF-300 nanoparticles obtained with the micellar approach but without the addition of aniline (see Table S5, Supporting Information). Indeed, the chemical composition (Figures S13, S14, and S15, Supporting Information) and surface area (Figure S16, Supporting Information) of this yellow powder were also found to be comparable to the COF-300 nanoparticles obtained with the micellar approach. Therefore, the data obtained confirm that the addition of aniline in the micellar media also facilitates the formation of COF-300 nanoparticles, even at the higher catalyst concentration. However, in sharp contrast to bulk synthetic approaches, the use of aniline in the micellar approach does not lead to an increased BET surface area or larger crystal sizes. Notably, these findings unequivocally illustrate the pivotal role of the CTAB/SDS mixed micelle core in the synthesis and controlled growth of COF-300 nanoparticles.

Capitalizing on the opportunities presented by the controlled confined synthesis within the hydrophobic micellar core, we conducted time-resolved DLS and small-angle X-ray scattering (SAXS) measurements during the formation of the colloidal solution to gain unprecedented insights into the growth mechanism of COF-300 at the nanoscale. We decided to study the growth mechanism of COF-300 nanoparticles in the absence of the modulator to simplify the reaction mechanism. As indicated above, the DLS analysis of the two micellar solutions containing the COF precursors give comparable results to those obtained for pure CTAB/SDS mixed micelles. However, upon mixing the two micellar solutions containing the COF precursors, and upon the

ADVANCED
SCIENCE NEWS

www.advancedsciencenews.com

ADVANCED
MATERIALS

www.advmat.de
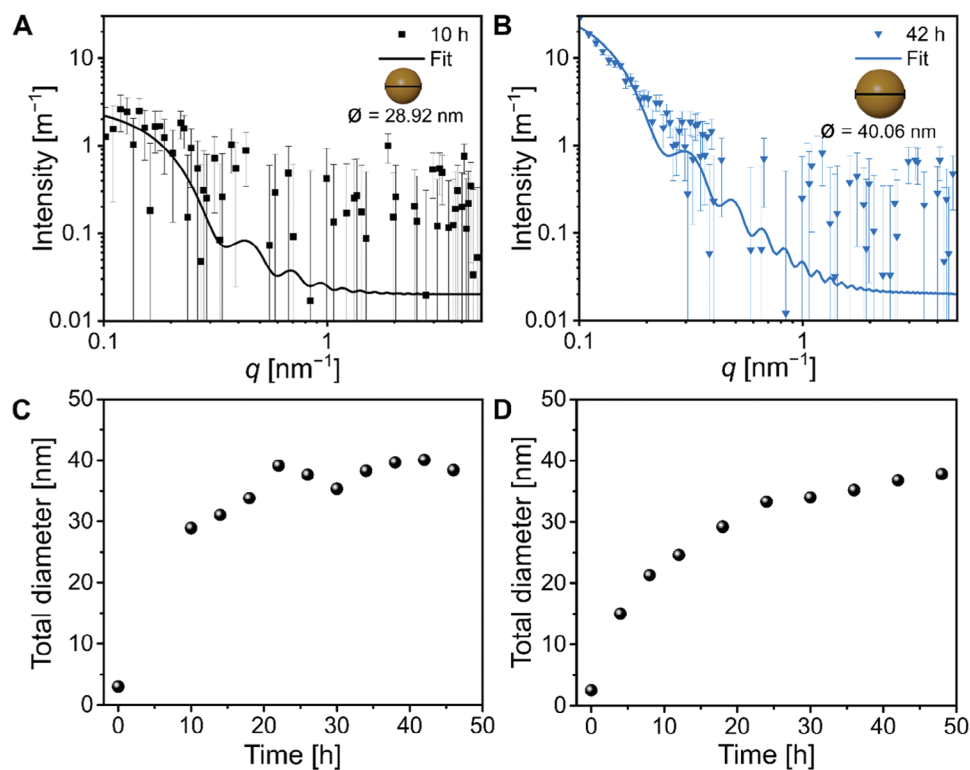
Figure 3. SAXS measurements of the colloidal solution of COF-300 nanoparticles at: A) 10 h (black) and B) 42 h (blue) after mixing the TAM and BDA precursors. C) Total diameter of the COF-300 nanoparticles over time according to the SAXS measurements (Figure S15, Supporting Information). D) Determined hydrodynamic diameter of COF-300 nanoparticles through DLS kinetics measurements, resulting in ≈40 nm spherical particles.

addition of the catalyst, notable changes in the DLS measurements and SAXS profiles were observed over time. Note that while the DLS measurements conducted on the reaction mixture showcased a progressive increase in the hydrodynamic diameter of the COF-300 nanoparticles over time, reaching a steady state at around 40 nm (**Figure 3D**), no substantial changes in the scattering profiles were obtained with the SAXS measurements during the initial 10 h of reaction. However, after 10 h of reaction clear changes in the SAXS spectra were also observed, allowing for the investigation of the growth mechanism of the COF-300 nanoparticles over time.[28,29] The SAXS scattering profiles obtained at two specific time points, namely the initial stage (10 h) and the final stage (42 h), are shown in Figure 3A,B, respectively. The obtained scattering values were subjected to fitting using a three-layer spherical model, comprising the core of the COF-300 nanoparticles, a hydrophobic layer that includes the alkyl chains of the surfactants, and a hydrophilic layer composed of the polar heads of the surfactants (more information of the model can be found in the Supporting Information). The fitting of the scattering profiles with the model clearly demonstrates an increase in intensity and a change in the slope at low scattering angles ($q < 1$ nm^{-1}) that indicate a progressive enlargement of the particle diameter from 29 to 40 nm during this time period accompanied by an increase of the volume fraction (see also Figure S17 and Table S6, Supporting Information). Accordingly, the model clearly shows that the growth of the COF-300 nanoparticles conforms better to an isotropic model that yields a maximum particle diameter of ≈40 nm after 48 h of reaction

(Figure 3C). Note that the growth mechanism observed for COF-300 nanoparticles using the micellar approach is significantly different from that of sub-20 nm 2D COF nanoparticles, produced following the same methodology. While in the case of COF-300 the SAXS scattering profiles better fit to a three-layer spherical model, sub-20 nm 2D COF nanoparticles revealed an anisotropic growth mechanism characterized by an initial lateral growth, resulting in a disk-like structure, followed by an increase in particle size perpendicular to the disk plane and driven by the $\pi-\pi$ stacking of 2D COF layers.[30–32] Undoubtedly, the hydrophobic micellar core offers a unique platform to explore and understand the intricacies of COF-300 synthesis and growth, paving the way for unprecedented possibilities in the realm of 3D COF research and beyond. Note that understanding the growth mechanism of crystals is crucial for controlling their size, structure, and consequently, their properties and functions, including processability. For instance, we have successfully demonstrated that the utilization of the micellar approach enables the formation of stable colloidal solutions of COF-300 nanoparticles under mild conditions, a feature that can enable their processability across scales and on multiple substrates and conditions, owing to its aqueous nature. To provide concrete evidence supporting this statement, we have employed the colloidal solution for the direct functionalization of complex 3D motile microstructures with COF-300 nanoparticles to create the first magnetic 3D COF-based microscale robots (COFBOTs).

In the context of microrobotics, COFs offer a unique canvas to introduce additional functionalities beyond locomotion due

**ADVANCED
SCIENCE NEWS**

www.advancedsciencenews.com

**ADVANCED
MATERIALS**

www.advmat.de
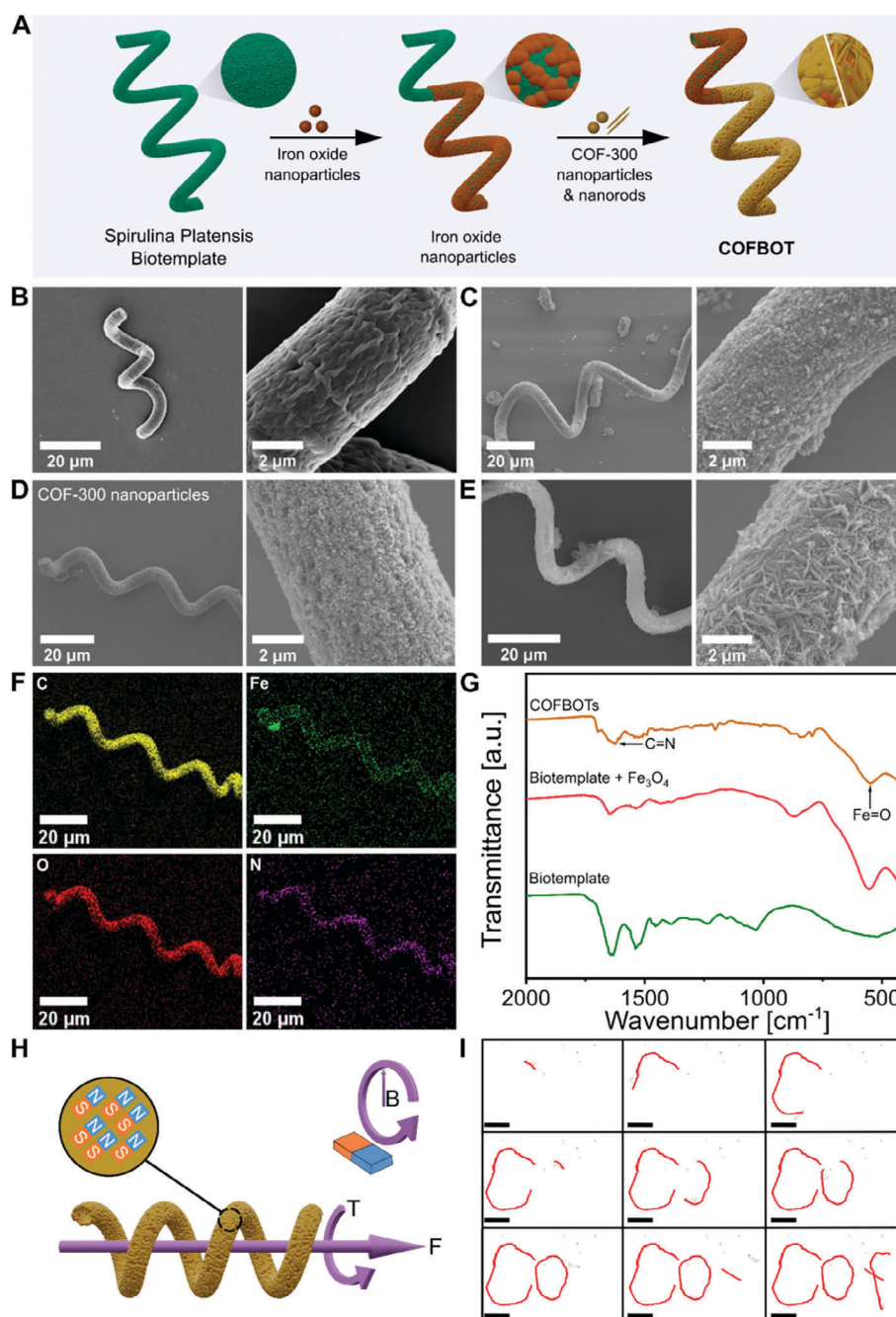
Figure 4. A) Illustration showing the fabrication steps of the COFBOTs following a biotemplate method. SEM images at different magnifications of: B) the helical biotemplate, C) the biotemplate coated with iron oxide nanoparticles, D) the microrobot coated with COF-300 nanoparticles, and E) the microrobot coated with the nanorods. F) EDX elemental mapping of a COFBOT coated with COF-300 nanoparticles, showcasing the carbon (yellow), iron (green), oxygen (red), and nitrogen (purple) distribution. G) ATR-FT-IR spectra of COFBOTs, depicting the C=N peak of the COF-300 and Fe=O peak corresponding to the Fe_3O_4. H) Schematic representation of the magnetic locomotion of the COFBOTs. I) Overlay of optical microscope images of a COFBOT following a user-defined path to spell the acronym "COF," by varying the magnetic field direction at 15 mT and 11 Hz (scale = 2 mm).

to their porous crystalline structures. This includes capabilities such as drug loading, biosensing, imaging, and combination therapy.[33] In addition, compared to porous crystalline metal–organic structures such as metal–organic frameworks (MOFs), COFs are generated via covalent bonds which increase their stability and form purely organic components making them promising candidates as biodegradable and biocompatible materials, crucial for applications requiring compatibility with cells and avoidance of immune response. It is important to acknowledge that while 3D COFs offer remarkable internal surface

**ADVANCED
SCIENCE NEWS**

www.advancedsciencenews.com

**ADVANCED
MATERIALS**

www.advmat.de

areas and pore sizes when compared to their 2D counterparts, the latter have received more attention as potential functional materials for small-scale swimmers.[34] This trace can be attributed to both the fact that synthesizing 2D COFs is relatively easier when compared to 3D COFs, as well as to the lack of synthetic approaches that can achieve a controlled generation of 3D COFs with nanoscale sizes. Nonetheless, limitations such as large particle size and the dependence on light propulsion hinder a broader use of the reported 2D COF-based microswimmers in the human body. Additionally, challenges arise from 2D COF synthesis in organic solvents or via solvothermal methods, posing integration difficulties with other small-scale devices and compatibility issues with other biomaterials.

Here, we demonstrate the successful integration of COF-300 nanoparticles into magnetic microrobots using our earlier reported biotemplating procedure (**Figure** 4A).[35] A helical-shaped *Spirulina platensis* was selected as a natural scaffold (Figure 4B) and subsequently coated with pre-synthesized Fe_3O_4 magnetic nanoparticles (Figure 4C) to confer magnetic functionality (see the Supporting Information for further details). Additionally, a glycerol/gelatin solution was used to coat the magnetic biotemplates with COF-300 nanoparticles. The COF-300 nanoparticles successfully adhered to the surface of the biotemplates, forming the COFBOTs. SEM images and energy-dispersive X-ray spectroscopy (EDX) maps confirmed the complete coverage of the magnetic biotemplate with the COF-300 nanoparticles (Figure 4D,F, respectively). Moreover, the COFBOTs were further analyzed by ATR-FTIR (Figure 4G) where the Fe─O stretching band at 580 cm^{-1}, which is a characteristic peak of iron oxide, was present in both the magnetized biotemplate and the COFBOT.[36] Additionally, the peak at 1616 cm^{-1} characteristic of COFs' C═N bonds, further confirms the adequate integration of the COF-300 nanoparticles onto the surface of the magnetic biotemplates. Importantly, note that this efficient and simple integration could be achieved by directly mixing the colloidal solution obtained via the mixed micelle method with the magnetic helical biotemplates and using ethanol for the precipitation of the COF-300 nanoparticles onto the magnetic biotemplate's surface. Significantly, this functionalization approach facilitates the fabrication sequence of COF-based microswimmers by avoiding additional processing of powders and redispersion steps. Furthermore, to showcase the versatility and reliability of this functionalization method, we also decided to utilize the colloidal dispersion of nanorods produced with our micellar approach. While one might anticipate a potential decrease in the coverage efficiency due to the change of the geometry from 0D to 1D nanostructures, we observed a uniform coating of the magnetic biotemplates with the nanorods throughout the entire helical structures (Figure 4E).

Unlike photocatalytic propelled swimmers, which exhibit random motion in solutions, the integration of COF-300 nanoparticles into magnetic 3D structures allows for controlled and guided motion. Due to the helical shape of the biotemplate and the incorporation of Fe_3O_4 nanoparticles, an external rotating magnetic field perpendicular to the long axis of the COFBOTs can induce a corkscrew rotating motion which translates into a net displacement of the COFBOTs in water (Figure 4H). At a rotating magnetic field of 15 mT and a frequency from 7 to 11 Hz, the COFBOTs start to move along the same axis. The minimum frequency required for corkscrew motion may vary among the microrobots

due to the inherent size inhomogeneity of the Spirulina biotemplate. In addition, a 100 mT m^{-1} out-of-plane gradient is applied to prevent the microrobots from contacting the surface of the microfluidic channel, hence enabling a straight-line motion of the COFBOTs at a velocity of 695 μm s^{-1} (Figure S16, Supporting Information). We further demonstrate that the COFBOTs can navigate along a user-defined path by changing both the direction and rotation frequency of the applied magnetic field, as seen in Figure 4I (Videos S1 and S2 show the real time locomotion of the COFBOTs, Supporting Information). Note that this controlled locomotion of COF-based microswimmers in 3D cannot be achieved with previously reported methods on 2D COF-based swimmers.

3. Conclusion

We have shown that the water-based nanoreactor technology presented here offers several advantages for 3D COF synthesis when compared to conventional synthetic methods. First, it enables the solubilization of COF-300 precursors in an aqueous medium, thereby simplifying the synthetic process by avoiding hazardous and toxic solvents. Second, it operates under mild conditions, such as room temperature and atmospheric pressure, ensuring energy efficiency and ease of implementation. Moreover, we have also demonstrated that this approach enables precise control over the synthesis and growth of COF-300 nanoparticles, a feature that is typically unachievable using conventional COF-based synthetic methods and that has proven to be key to improve processability. We believe that this achievement will also have an important impact on the application and utilization of 3D COFs with nanoscale dimensions, enabling their seamless integration and application in domains that were previously inaccessible with large crystal structures. Particularly, this breakthrough holds the potential to revolutionize areas such as 3D COFs for nano/microrobotic applications and biomedicine, further emphasizing the significance of our findings.

Supporting Information

Supporting Information is available from the Wiley Online Library or from the author.

Conflict of Interest

The authors declare no conflict of interest.

Data Availability Statement

The data that support the findings of this study are available from the corresponding author upon reasonable request.

Keywords

3D COFs, crystal growth, micelles, microrobots, nanoreactor technology, processability

[1] F. Barthelat, *Philos. Trans. R. Soc., A* **2007**, *365*, 2907.

[2] X. J. Ma, T. F. Scott, *Commun. Chem.* **2018**, *1*, 98.

[3] L. Bourda, C. Krishnaraj, P. Van Der Voort, K. Van Hecke, *Mater. Adv.* **2021**, *2*, 2811.

[4] S.-Y. Ding, W. Wang, *Chem. Soc. Rev.* **2013**, *42*, 548.

[5] A. P. Cote, A. I. Benin, N. W. Ockwig, M. O'keeffe, A. J. Matzger, O. M. Yaghi, *Science* **2005**, *310*, 1166.

[6] O. M. Yaghi, M. J. Kalmutzki, C. S. Diercks, *Introduction to Reticular Chemistry: Metal-Organic Frameworks and Covalent Organic Frameworks*, Wiley-VCH, Weinheim **2019**, p. 1.

[7] F. Haase, B. V. Lotsch, *Chem. Soc. Rev.* **2020**, *49*, 8469.

[8] W. Zhang, L. Chen, S. Dai, C. Zhao, C. Ma, L. Wei, M. Zhu, S. Y. Chong, H. Yang, L. Liu, Y. Bai, M. Yu, Y. Xu, X.-W. Zhu, Q. Zhu, S. An, R. S. Sprick, M. A. Little, X. Wu, S. Jiang, Y. Wu, Y.-B. Zhang, H. Tian, W.-H. Zhu, A. I. Cooper, *Nature* **2022**, *604*, 72.

[9] J. W. Colson, A. R. Woll, A. Mukherjee, M. P. Levendorf, E. L. Spitler, V. B. Shields, M. G. Spencer, J. Park, W. R. Dichtel, *Science* **2011**, *332*, 228.

[10] J. Kim, A. Elabd, S.-Y. Chung, A. Coskun, J. W. Choi, *Chem. Mater.* **2020**, *32*, 4185.

[11] Y. Zhao, L. Guo, F. Gándara, Y. Ma, Z. Liu, C. Zhu, H. Lyu, C. A. Trickett, E. A. Kapustin, O. Terasaki, O. M. Yaghi, *J. Am. Chem. Soc.* **2017**, *139*, 13166.

[12] F. J. Uribe-Romo, C. J. Doonan, H. Furukawa, K. Oisaki, O. M. Yaghi, *J. Am. Chem. Soc.* **2011**, *133*, 11478.

[13] S. Kandambeth, K. Dey, R. Banerjee, *J. Am. Chem. Soc.* **2019**, *141*, 1807.

[14] X. Y. Xu, R. Xiong, Z. N. Zhang, X. J. Zhang, C. L. Gu, Z. C. Xu, S. L. Qiao, *Chem. Eng. J.* **2022**, *447*, 137447.

[15] R. Liu, K. T. Tan, Y. Gong, Y. Chen, Z. Li, S. Xie, T. He, Z. Lu, H. Yang, D. Jiang, *Chem. Soc. Rev.* **2021**, *50*, 120.

[16] T. Ma, E. A. Kapustin, S. X. Yin, L. Liang, Z. Zhou, J. Niu, L.-H. Li, Y. Wang, J. Su, J. Li, X. Wang, W. D. Wang, W. Wang, J. Sun, O. M. Yaghi, *Science* **2018**, *361*, 48.

[17] W. Ji, D. M. Kim, B. M. Posson, K. J. Carlson, A. C. Chew, A. J. Chew, M. Hossain, A. F. Mojica, S. M. Ottoes, D. V. Tran, M. W. Greenberg, L. S. Hamachi, *RSC Adv.* **2023**, *13*, 14484.

[18] Q. Fang, J. Wang, S. Gu, R. B. Kaspar, Z. Zhuang, J. Zheng, H. Guo, S. Qiu, Y. Yan, *J. Am. Chem. Soc.* **2015**, *137*, 8352.

[19] K. Wang, W. J. Wang, S. H. Pan, Y. M. Fu, B. Dong, H. Wang, *Appl. Mater. Today* **2020**, *19*, 100550.

[20] V. Tomasic, I. Stefanic, N. Filipovic-Vincekovic, *Colloid Polym. Sci.* **1999**, *277*, 153.

[21] J. Á. Martín-Illán, D. Rodríguez-San-Miguel, C. Franco, I. Imaz, D. Maspoch, J. Puigmartí-Luis, F. Zamora, *Chem. Commun.* **2020**, *56*, 6704.

[22] B. J. Smith, A. C. Overholts, N. Hwang, W. R. Dichtel, *Chem. Commun.* **2016**, *52*, 3690.

[23] B. H. Toby, R. B. Von Dreele, *J. Appl. Crystallogr.* **2013**, *46*, 544.

[24] G. S. Pawley, *J. Appl. Crystallogr.* **1981**, *14*, 357.

[25] F. J. Uribe-Romo, J. R. Hunt, H. Furukawa, C. Klöck, M. O'keeffe, O. M. Yaghi, *J. Am. Chem. Soc.* **2009**, *131*, 4570.

[26] T. Ma, J. Li, J. Niu, L. Zhang, A. S. Etman, C. Lin, D. Shi, P. Chen, L.-H. Li, X. Du, J. Sun, W. Wang, *J. Am. Chem. Soc.* **2018**, *140*, 6763.

[27] R. A. Dodson, J. Park, J. Kim, M. J. Cliffe, S. M. Cohen, *Inorg. Chem.* **2022**, *61*, 12284.

[28] D. Orthaber, A. Bergmann, O. Glatter, *J. Appl. Crystallogr.* **2000**, *33*, 218.

[29] J. S. Pedersen, *Adv. Colloid Interface Sci.* **1997**, *70*, 171.

[30] C. Franco, D. Rodríguez-San-Miguel, A. Sorrenti, S. Sevim, R. Pons, A. E. Platero-Prats, M. Pavlovic, I. Szilágyi, M. L. Ruiz Gonzalez, J. M. González-Calbet, D. Bochicchio, L. Pesce, G. M. Pavan, I. Imaz, M. Cano-Sarabia, D. Maspoch, S. Pané, A. J. De Mello, F. Zamora, J. Puigmartí-Luis, *J. Am. Chem. Soc.* **2020**, *142*, 3540.

[31] B. J. Smith, L. R. Parent, A. C. Overholts, P. A. Beaucage, R. P. Bisbey, A. D. Chavez, N. Hwang, C. Park, A. M. Evans, N. C. Gianneschi, W. R. Dichtel, *ACS Cent. Sci.* **2017**, *3*, 58.

[32] S. Thomas, H. Li, C. Zhong, M. Matsumoto, W. R. Dichtel, J.-L. Bredas, *Chem. Mater.* **2019**, *31*, 3051.

[33] Y. Q. Shi, F. Gao, Q. C. Zhang, J. L. Yang, *ACS Nano* **2023**, *17*, 1879.

[34] V. Sridhar, E. Yildiz, A. Rodríguez-Camargo, X. Lyu, L. Yao, P. Wrede, A. Aghakhani, B. M. Akolpoglu, F. Podjaski, B. V. Lotsch, M. Sitti, *Adv. Mater.* **2023**, 2301126.

[35] A. Terzopoulou, M. Palacios-Corella, C. Franco, S. Sevim, T. Dysli, F. Mushtaq, M. Romero-Angel, C. Marti-Gastaldo, D. Gong, J. Cai, X.-Z. Chen, M. Pumera, A. J. Demello, B. J. Nelson, S. Pané, J. Puigmarti-Luis, *Adv. Funct. Mater.* **2022**, *32*, 2107421.

[36] Y. Li, C.-X. Yang, X.-P. Yan, *Chem. Commun.* **2017**, *53*, 2511.